Manipulation of Nanoscale Intergranular Phases for High Proton Conduction and Decomposition Tolerance in BaCeO₃ Polycrystals

Hye-Sung Kim,[†] Hyung Bin Bae,[‡] WooChul Jung,[§] and Sung-Yoon Chung*[,†]

[†]Graduate School of EEWS, [‡]KAIST Analysis Center, and [§]Department of Materials Science and Engineering, Korea Advanced Institute of Science and Technology (KAIST), Daejeon 34141, Korea

S *Supporting Information*

ABSTRACT: In many ion-conducting polycrystalline oxides, grain boundaries are generally accepted as rate-limiting obstacles to rapid ionic diffusion, often resulting in overall sluggish transport. Consequently, based on a precise understanding of the structural and compositional features at grain boundaries, systematic control of the polycrystalline microstructure is a key factor to achieve better ionic conduction performance. In this study, we clarify that a nanometer-thick amorphous phase at most grain boundaries in proton-conducting BaCeO₃ polycrystals is responsible for sub-stantial retardation of proton migration and moreover is very reactive with water and carbon dioxide gas. By a combination of atomic-scale chemical analysis and physical imaging, we demon-

strate that highly densified BaCeO₃ polycrystals free of a grain-boundary amorphous phase can be easily fabricated by a conventional ceramic process and show sufficiently high proton conductivity together with significantly improved chemical stability. These findings emphasize the value of direct identification of intergranular phases and subsequent manipulation of their distribution in ion-conducting oxide polycrystals.

KEYWORDS: *Electrolytes, grain boundaries, ionic conduction, perovskite oxides, TEM*
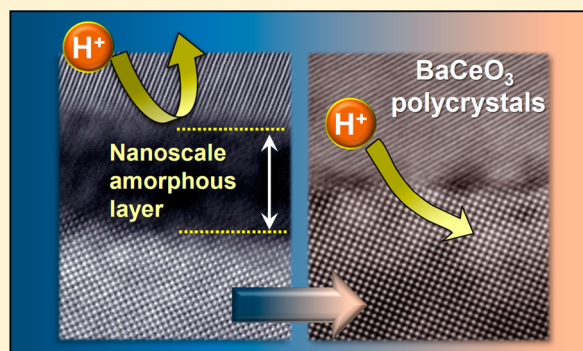
Since the first reports on the high-temperature proton conduction behavior discovered in SrCeO₃ in the early 1980s,[1,2] a substantial amount of works on the perovskite-type proton-conducting oxides have been carried out to elucidate the incorporation process of protons during hydration, the conduction mechanism and path in the lattice, and the correlation between vacancies and dopants from a defect chemical viewpoint.[3−12] Although initial studies largely dealt with SrCeO₃, a notable report[3] in 1988 on the significantly high proton conductivity in BaCeO₃ led to many relevant follow-up research to the Ba-based perovskites.[4,6−12] As a result, a variety of electrolyte membrane applications at elevated temperatures have been proposed in solid-oxide fuel cells, in steam electrolyzers for hydrogen production, and even in electro-chemical cell reactors for methane conversion to versatile hydrocarbon materials.[13−17]

Despite the outstanding ionic conductivity of BaCeO₃[18] among many perovskite-type proton conductors, the chemical instability of the cerate under moisture- and CO₂-rich environments has been noted as a major drawback,[19−23] revealing the formation of barium hydroxides and carbonates. As such circumstances can be similar to the real operation conditions of fuel cells and electrolyzers, this instability has prevented BaCeO₃ from extensive utilization as effective electrolyte membranes. BaZrO₃ has accordingly garnered considerable attention since the late 1990s,[6] as it is chemically fairly robust and consequently is not easily decomposed into other phases. However, because of the enormously high sintering temperature, usually more than 1600 °C to obtain a dense microstructure, BaZrO₃ polycrystals are not compatible with the relatively lower processing temperature of materials for electrodes.

Highly resistive grain boundaries,[24−28] compared with bulk grains, are another significant shortcoming that should be overcome in the Ba-based perovskites to achieve sufficient conduction performance. Including solid solutions with multi-ple cations,[13,16,29] the development of micron-scale thin films,[30] the fabrication of textured and epitaxially oriented films by pulsed laser deposition,[31] and even the suggestion of completely new perovskite composition, for example, SmNiO₃,[32] several notable experimental methods have been proposed over the past decade to overcome the major barriers encountered with perovskite proton conductors. Although significant performance leaps have been achieved in thin-film technologies and crucial insights into alternative ways of fabrication have been presented, control of polycrystalline microstructure on the basis of the conventional ceramic technique is still a key process to manufacture oxide electrolyte membranes at a large scale.

In this work, we show that dense $BaCeO_3$ polycrystals presenting both significantly reduced grain-boundary impedance and notably enhanced tolerance to decomposition can be fabricated via a traditional sintering process. Focusing on $BaCeO_3$ doped with trivalent acceptor cations (Ba-$Ce_{1-x}M_xO_{3-\delta}$, where M = Dy, Gd, Sm, Y), we first clarify that nanoscale Ba-excess intergranular amorphous phases are present at most grain boundaries in sintered polycrystals. By using two straightforward experimental approaches, we successfully demonstrate that polycrystalline samples consisting of intergranular-phase-free grain boundaries reveal remarkable improvements of both proton conduction and chemical stability under CO_2- and H_2O-rich environments. Reopening a new possibility of $BaCeO_3$ utilization for dense electrolyte membranes fabricated via a simple ceramic process by sintering, the findings in the present study highlight that suppressing intergranular amorphous phases at grain boundaries together with the highly densified microstructure is a key challenge to attain notable proton conduction and phase stability against decomposition at the same time.

During the scanning transmission electron microscopy (STEM) observation, we could easily identify the presence of a thin secondary phase exhibiting a different image contrast at most grain boundaries in polycrystalline $BaCe_{1-x}M_xO_{3-\delta}$ (M = Dy, Gd, Sm, Y). Figure 1a shows the typical polycrystalline
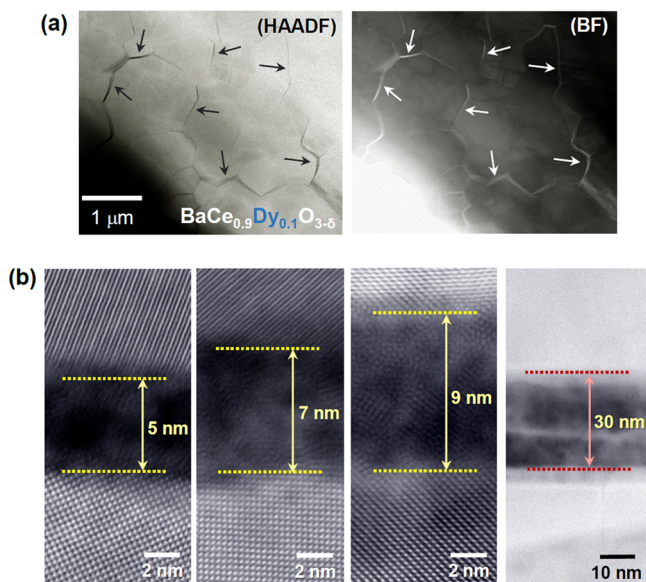

Figure 1. Polycrystalline microstructure and nanoscale intergranular phases. (a) Both HAADF and corresponding BF STEM images acquired in $BaCe_{0.9}Dy_{0.1}O_{3-\delta}$ polycrystals exemplify the presence of intergranular layers at most of grain boundaries, as indicated by arrows. (b) A series of HAADF images demonstrates that the thickness of intergranular layers varies from a few nanometers up to tens of nanometers. An amorphous nature of the layers can be also identified in the third image at an atomic level, exhibiting merely the short-range order.

microstructure of $BaCe_{0.9}Dy_{0.1}O_{3-\delta}$ sintered at 1400 °C. As indicated by arrows in both high-angle annular dark-field (HAADF) and bright-field (BF) images, a thin intergranular phase is readily recognizable. When grain boundaries in sintered samples were scrutinized by STEM at higher magnification, two notable structural features could be found. One is that the thickness of intergranular layers is in a

somewhat wide range, varying from a few nanometers up to several tens of nanometers, as exemplified in a set of HAADF images in Figure 1b. Therefore, the amount of the secondary phase at grain boundaries does not appear to be negligible although it is difficult to precisely quantify merely by STEM observation. The other important aspect is that the intergranular layers are amorphous. As can be seen in Figure 1b, the amorphous nature of the layers is observable in HAADF images. BF images also clearly verify the amorphous state of the intergranular layers,[33,34] showing a short-range structural order at an angstrom scale (also see Figure S1 in Supporting Information).

It should be noted that such an intergranular phase is also identified even in pristine $BaCeO_3$ polycrystals sintered at 1400 °C despite the stoichiometric cation composition of Ba/Ce = 1. Consequently, the presence of a secondary amorphous phase does not pertain to the addition of acceptors but appears to stem from the intrinsic phase relation of $BaCeO_3$ as a thermodynamically stable configuration. We thus carried out chemical composition analyses on both intergranular amorphous phases and bulk grains to understand the phase equilibrium and resultant formation of second phases. Figure 2a shows the chemical maps of Ba and Ce for a triple junction region obtained in pristine $BaCeO_3$ by energy-dispersive X-ray spectroscopy (EDS). As demonstrated in the HAADF image in the left-hand column, a ~20 nm thick intergranular phase is present at all three grain boundaries as well as in the junction. This set of EDS maps directly indicates that the intergranular phase is significantly Ce-deficient while a Ba X-ray signal is sufficiently detected in the map. Very consistent EDS results are also verified in $BaCe_{0.9}Dy_{0.1}O_{3-\delta}$ and $BaCe_{0.9}Gd_{0.1}O_{3-\delta}$ samples (see Figure S2), revealing that the thin second phase observed at grain boundaries in each of the samples is a Ba-rich amorphous oxide.

Another noticeable finding on the chemical composition originates from the bulk. Figure 2b presents a set of atomic-column-resolved EDS maps acquired from a bulk grain in the [100] projection in a $BaCe_{0.9}Gd_{0.1}O_{3-\delta}$ sample. Note that Ba and Ce columns are not distinguishable in the HAADF image, because their atomic numbers (Z) do not significantly differ with each other (Z_{Ba} = 56 and Z_{Ce} = 58). In contrast, the atomic-scale EDS maps clearly discriminate each of the columns for Ba and Ce (blue and red maps, respectively) and furthermore clarify that most Gd dopants are substituted for Ce (yellow map), as intended from the initial composition. A more important but unexpected aspect in Figure 2b is that a substantial Ce signal beyond the background noise is detectable at the Ba sites, as indicated by a white arrow in the Ce map, whereas no significant Ba signal comes from the Ce sites. An additional set of EDS maps for the $BaCe_{0.9}Gd_{0.1}O_{3-\delta}$ sample is provided in Supporting Figure S3 for verification. In addition, this Ce intermixing into the Ba sites is consistently observed in pristine $BaCeO_3$ as well (see Figure S4), representing that the mixed occupancy by Ce is a thermodynamically favorable configuration at elevated temperature. On the basis of our quantitative analysis by the acquisition of sufficient X-ray signals from more than five grains in each sample (see Experimental details in Supporting Information), the Ce concentration at the Ba site was determined to be 3−5% for each sample (see Figure S5).

Along with the STEM images provided in Figure 1, the two sets of EDS results shown in Figure 2a,b prove that $BaCeO_3$ has a small degree of Ce occupancy at the Ba site. Consequently, if
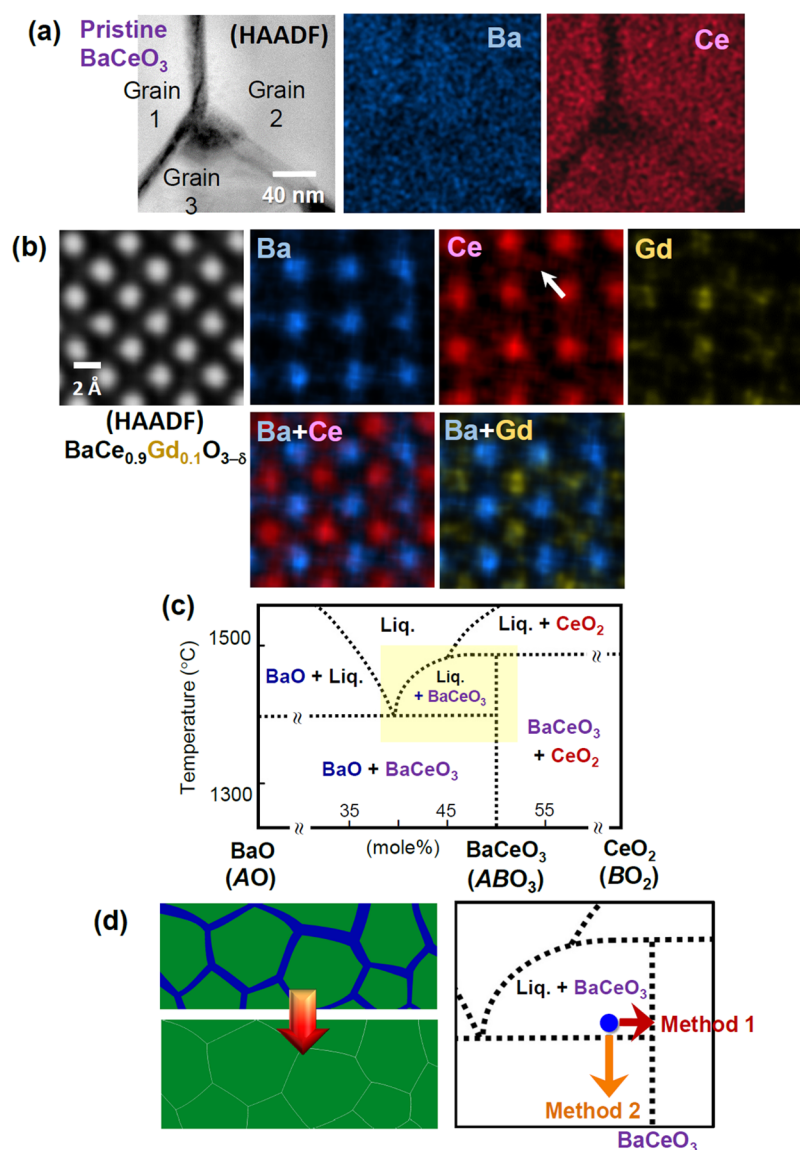
Figure 2. EDS analyses and phase-equilibrium relation in $BaCeO_3$. (a) This pair of EDS maps for Ba and Ce along with the HAADF image verifies the relatively Ba-rich and Ce deficient composition of an intergranular phase as well as demonstrates the presence of the secondary phase at grain boundaries even in pristine stoichiometric $BaCeO_3$. (b) In this set of atomic-column-resolved EDS maps, intermixing of Ce into the Ba sites is directly revealed, as indicated by a white arrow in the Ce map. (c) The relevant phase diagram between BaO and CeO_2 is provided on the basis of a previous report.[35] The yellow shadow denotes the narrow two-phase region explaining the existence of a Ba-rich liquid phase in the microstructure. (d) Two distinct methods are suggested to suppress the formation of an amorphous phase and thereby to achieve the intergranular-phase-free microstructure by simple sintering, as schematically depicted in the left panel.

the starting composition is set to be Ba/Ce = 1 to fabricate polycrystalline $BaCeO_3$, this always leads to Ba-site-excess (or A-site-excess) nonstoichiometry, thereby resulting in the formation of Ba-rich secondary phases. In addition to the STEM and EDS analyses, the phase diagram between BaO and CeO_2 consistently indicates the presence of a substantial amount of Ba-excess amorphous phase, although this diagram was fairly roughly determined in 1971.[35] As denoted by a yellow shadow in Figure 2c, the compositional width of the two-phase region consisting of liquid−$BaCeO_3$ is considerably narrow. As a result, even a small degree of Ba-site-cation-excess nonstoichiometry can induce the formation of a significant amount of a liquid phase, based on the well-known lever rule applied to a two-phase region in a binary phase diagram. The large blue point in the magnified phase diagram on the right-

hand side in Figure 2d schematically represents the virtual composition of our samples.

It is generally accepted that grain boundaries in polycrystalline microstructure act as major barriers retarding rapid proton conduction.[24−26] In this regard, the presence of intergranular amorphous secondary phases shown in this work is reasonably anticipated to seriously deteriorate the fast conduction of protons through the grain boundaries. As schematically illustrated in Figure 2d, we thus suggest two approaches to efficiently suppress the formation of Ba-rich amorphous phases at grain boundaries. The first method is to adjust the starting Ba/Ce ratio of samples so that the initial composition, denoted by the blue point in the phase diagram, horizontally shifts out of the two-phase region, as indicated by a red arrow. To this end, we prepare 5%-Ba-deficient samples of $Ba_{0.95}Ce_{1-x}M_xO_{3-\delta}$ by taking the Ce concentration of 3−5% at the Ba site into
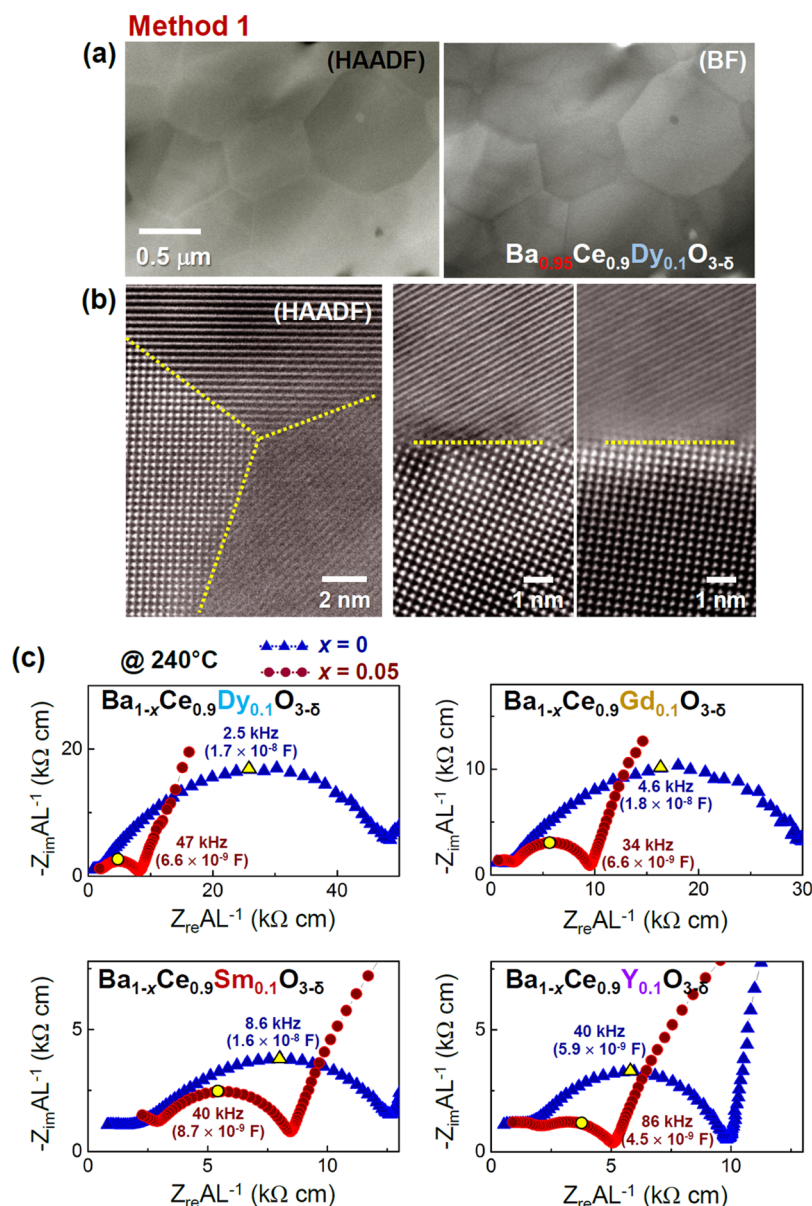
Figure 3. Control of Ba-deficient nonstoichiometry (Method 1). (a) Both HAADF and corresponding BF STEM images show the typical polycrystalline structure of well-densified $Ba_{0.95}Ce_{0.9}Dy_{0.1}O_{3-\delta}$ without intergranular amorphous phases. (b) At a higher magnification in HAADF mode, grain boundaries are clearly confirmed to be free of thin amorphous layers, showing direct grain–grain contacts, as denoted by yellow broken lines. (c) Notably reduced grain-boundary impedance is consistently measured in all of Ba-deficient $Ba_{0.95}Ce_{0.9}M_{0.1}O_{3-\delta}$ (red curves), compared with that of stoichiometric $BaCe_{0.9}M_{0.1}O_{3-\delta}$ (blue curves), where M = Dy, Gd, Sm, Y.

consideration, as shown in Figure S5. The second method is to postanneal the samples having intergranular amorphous phases at lower temperature. This approach is equivalent to a vertically downward shift of the blue point out of the liquid–BaCeO₃ two-phase region in order to avoid the formation of a liquid phase, as indicated by an orange arrow. Although postannealing at lower temperature leads the overall phase equilibrium into another two-phase region of BaO–BaCeO₃, the influence of the secondary BaO phase on the grain-boundary conduction is expected to be marginal, as the amount of this phase should be remarkably reduced on the basis of the lever rule in the BaO–BaCeO₃ two-phase region.

For the first approach, 5%-Ba-deficient $Ba_{0.95}Ce_{0.9}M_{0.1}O_{3-\delta}$ samples doped with 10% acceptors (M = Dy, Gd, Sm, Y) were sintered at 1400 °C for 5 h. Figure 3a exemplifies the typical microstructure of $Ba_{0.95}Ce_{0.9}Dy_{0.1}O_{3-\delta}$ acquired in STEM. A

highly densified polycrystalline microstructure showing no intergranular phases is easily observed in the figures. Atomic-level HAADF images in Figure 3b also confirm that grain boundaries and triple junctions are free of amorphous phases. When the STEM images shown in Figure 1a,b are compared with those in Figures 3a,b, it is readily recognized that the 5%-Ba-deficient composition adjustment is very effective to suppress the formation of intergranular amorphous phases in excellent agreement with the phase equilibrium from the phase diagram. In addition, atomic-column-resolved EDS maps obtained in $Ba_{0.95}Ce_{0.9}Dy_{0.1}O_{3-\delta}$ invariably reveal Ce occupancy at the Ba sites (see Figure S6), verifying that the intermixed occupation by Ce in the bulk is not affected by the initial cation nonstoichiometry. The most significant feature in each set of sintered $Ba_{0.95}Ce_{0.9}M_{0.1}O_{3-\delta}$ samples is that the grain boundary impedance remarkably diminishes. Figure 3c
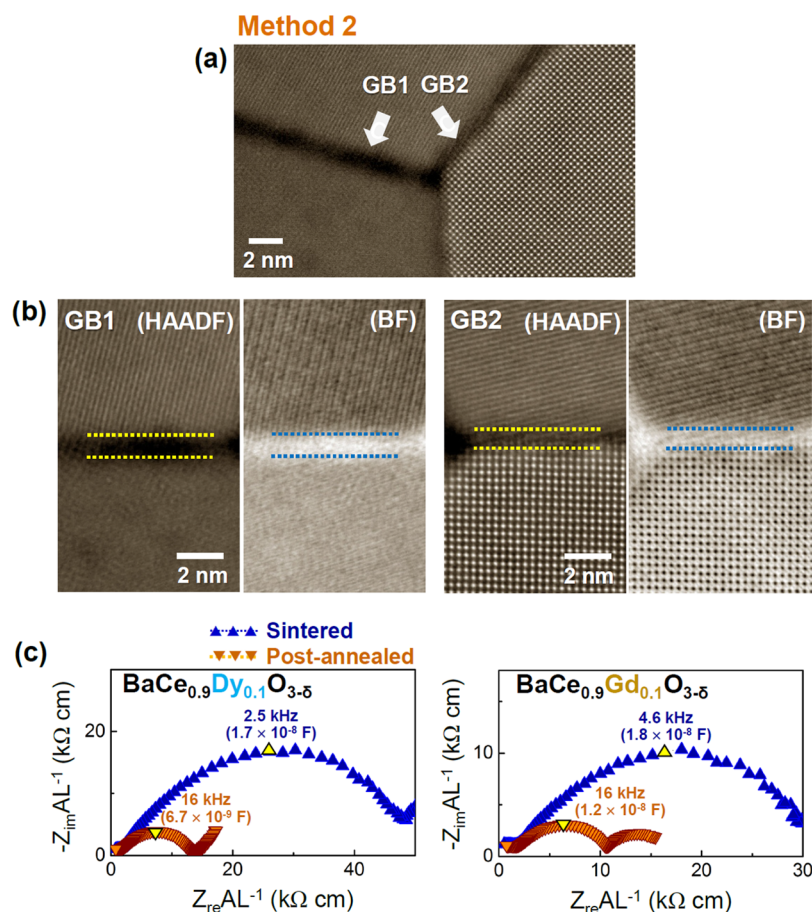
Figure 4. Postannealing at 1150 °C for 100 h (Method 2). (a) This HAADF image shows that very thin layers (white arrows) remain at grain boundaries after postannealing of $BaCe_{0.9}Dy_{0.1}O_{3-\delta}$. (b) As denoted by each pair of broken lines, less than 2 nm thick amorphous layers are identified in these sets of magnified images for the regions of GB1 and GB2. Therefore, very sluggish kinetics at such a low temperature, 1150 °C, appears to hinder the redistribution and subsequent conversion of the Ba-rich liquid phase into a solid phase. (c) Both Nyquist plots also verify the significantly reduced grain-boundary impedance in the postannealed samples in accord with the STEM observation demonstrating much thinner intergranular layers in (a).

compares the impedance results between $BaCe_{0.9}M_{0.1}O_{3-\delta}$ and $Ba_{0.95}Ce_{0.9}M_{0.1}O_{3-\delta}$. The diameter of the second arc in each $Ba_{0.95}Ce_{0.9}M_{0.1}O_{3-\delta}$ (red curves) is much smaller than that in $BaCe_{0.9}M_{0.1}O_{3-\delta}$ (blue curves) in the Nyquist plots, directly indicating significantly lower grain-boundary impedance in all the Ba-deficient samples. We also verified an additional reduction of the grain-boundary impedance when a higher doping concentration, 15%, of acceptors was introduced in Ba-deficient samples of $Ba_{0.95}Ce_{0.85}M_{0.15}O_{3-\delta}$ (see Figure S7).

For the second experimental approach, we postannealed the 1400 °C-sintered samples of $BaCe_{0.9}M_{0.1}O_{3-\delta}$ at a much lower temperature, 1150 °C, for a long period of time, 100 h. Figure 4a shows grain boundaries connected by a triple junction in postannealed $BaCe_{0.9}Dy_{0.1}O_{3-\delta}$. As provided in the enlargements in Figure 4b for the grain boundaries of GB1 and GB2, most intergranular phases were identified to become much thinner, compared with those shown in Figure 1. The presence of a-few-nanometer-thick residual amorphous layers implies that the overall sample has not reached the BaO−BaCeO$_3$ two-phase equilibrium due to much sluggish kinetics at the comparatively low postannealing temperature. Nevertheless, as directly compared in Figure 4c, the grain-boundary impedance of each sample is demonstrated to be significantly lower after postannealing (orange curves). In accord with the first approach, this second method thus provides consistent and

compelling evidence for a correlation between the suppression of Ba-rich intergranular amorphous phases and the critical reduction of grain-boundary impedance. To provide statistical information, the thickness of an intergranular phase in Dy-doped samples was measured at approximately 30−100 grain boundaries in each of the $BaCe_{0.9}Dy_{0.1}O_{3-\delta}$, $Ba_{0.95}Ce_{0.9}Dy_{0.1}O_{3-\delta}$, and postannealed $BaCe_{0.9}Dy_{0.1}O_{3-\delta}$ specimens during the STEM analysis. Much thinner intergranular amorphous phases (3 nm in average thickness) by postannealing are clearly verified in a series of bar graphs in Figure S8. Sets of STEM images exemplifying the variation of the thickness in the three samples are also provided in Figure S9.

To examine the influence of intergranular amorphous phases on the activation energies of ionic migration, we measured the variation of proton conductivity as a function of temperature. Figure 5 shows the Arrhenius-type plots of sintered samples with and without intergranular phases controlled by the Ba nonstoichiometry, as demonstrated in the first approach. Not only showing the enhancement of the conductivity, each of the $Ba_{0.95}Ce_{0.9}M_{0.1}O_{3-\delta}$ samples without intergranular phases coherently exhibits a notable decrement in the activation energy. Therefore, along with the two sets of experimental results in Figures 3 and 4, the lower activation barrier revealed in the $Ba_{0.95}Ce_{0.9}M_{0.1}O_{3-\delta}$ samples strongly supports the significance of controlling the intergranular phases in
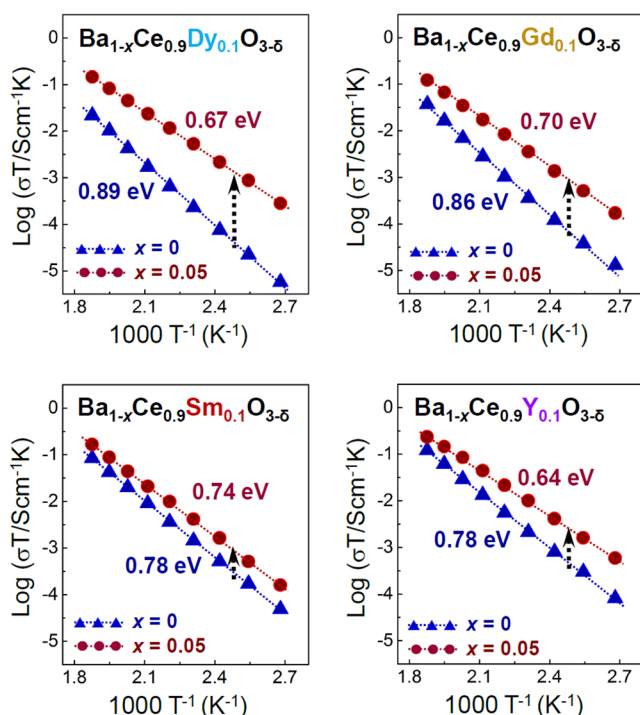
Figure 5. Arrhenius plots of grain-boundary conductivities measured by the impedance spectroscopy. A distinct reduction of the activation energy value in each Ba-deficient $Ba_{0.95}Ce_{0.9}M_{0.1}O_{3-\delta}$ sample is noted in addition to the enhanced conductivities, indicating much easier transport of protons through grain boundaries.

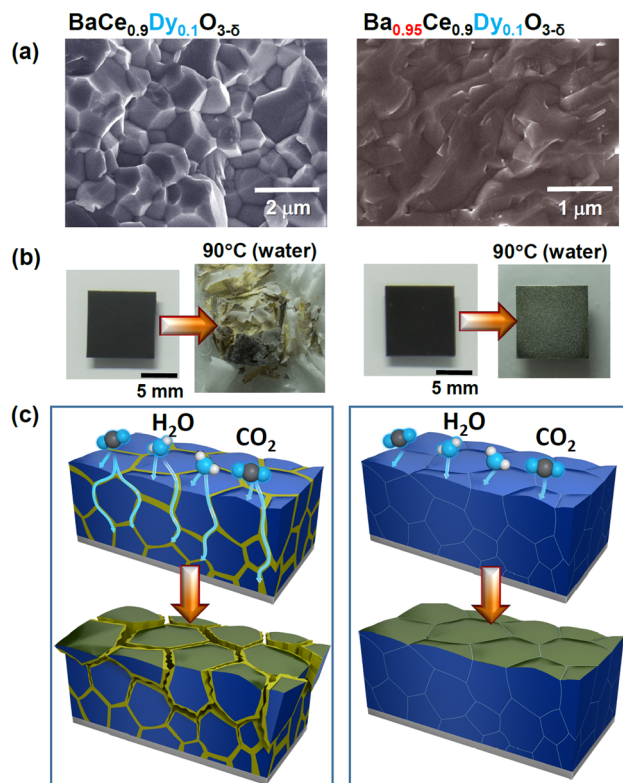**Figure 6.** Comparison of structural variation between stoichiometric $BaCe_{0.9}Dy_{0.1}O_{3-\delta}$ and Ba-deficient $Ba_{0.95}Ce_{0.9}Dy_{0.1}O_{3-\delta}$ samples. (a) Completely different fracture morphologies are readily observed. While the intergranular fracture behavior is shown in the stoichiometric sample (left), it is difficult to identify the position of grain boundaries in the Ba-deficient sample (right) in accord with the transgranular fracture characteristics. (b) The sintered microstructure of stoichiometric $BaCe_{0.9}Dy_{0.1}O_{3-\delta}$ rapidly collapses when annealed at 90 °C into water for 3 h, resulting in serious subsequent decomposition (left). In contrast, the Ba-deficient $Ba_{0.95}Ce_{0.9}Dy_{0.1}O_{3-\delta}$ sample shows notable durability against water even after 9 h at 90 °C (right). (c) This set of schematic illustrations describes that the intergranular amorphous phases act as a rapid penetration path of H_2O and CO_2 molecules and thus facilitates the structural decomposition.

BaCeO$_3$-based polycrystals to attain low impedance for easier proton conduction. Additional impedance measurements without protons by hydration were carried out to verify the electronic contribution is negligible and thus the overall conduction is based on the proton ions (see Figure S10).

We identified completely different fracture behavior depending on whether an intergranular amorphous phase is present at grain boundaries. As compared in Figure 6a by the example of Dy-doped samples, a well-developed grain structure is easily observed on the fractured surface in $BaCe_{0.9}M_{0.1}O_{3-\delta}$ (left), whereas it is not possible to discriminate each of the grain boundaries in the microstructure of Ba-deficient $Ba_{0.95}Ce_{0.9}M_{0.1}O_{3-\delta}$ (right). This typical difference in fracture morphology directly indicates that the fracture preferentially takes place along the intergranular amorphous phase at grain boundaries in $BaCe_{0.9}M_{0.1}O_{3-\delta}$, in contrast to the transgranular random fracture in Ba-deficient $Ba_{0.95}Ce_{0.9}M_{0.1}O_{3-\delta}$ (see Figure S11 for schematic illustrations describing the two different fracture modes). As a result, a much weaker bonding state in the grain-boundary amorphous phase than that in the crystalline grains is reasonably inferred.

In addition to the mechanical fragility, the intergranular amorphous phase was found to be significantly reactive with water and CO_2. For a more realistic comparison, sintered polycrystalline pellets with a sufficiently high relative density (>98%) were used in the chemical stability tests. Figure 6b shows the optical micrographs of sintered $BaCe_{0.9}Dy_{0.1}O_{3-\delta}$ (left) and Ba-deficient $Ba_{0.95}Ce_{0.9}Dy_{0.1}O_{3-\delta}$ (right) after each sample is submerged in water at 90 °C. While a remarkable collapse of sintered microstructure and subsequent decomposition into $BaCO_3$ and $Ba(OH)_2·H_2O$ can be found in $BaCe_{0.9}Dy_{0.1}O_{3-\delta}$ (left) after 3 h, the initial shape of the

sintered pellet is notably preserved for a much longer time (>13 h) without substantial decomposition in $Ba_{0.95}Ce_{0.9}Dy_{0.1}O_{3-\delta}$ (right) (see Figure S12 for the time-dependent morphology variations of a sintered sample). A consistent comparison of morphology variations between $BaCe_{0.9}Gd_{0.1}O_{3-\delta}$ and $Ba_{0.95}Ce_{0.9}Gd_{0.1}O_{3-\delta}$ is also demonstrated in Figure S13, to verify the noticeable durability of the Ba-deficient samples (see all the X-ray diffraction results for the crushed samples after the reaction with water in Figure S14 as well as the X-ray diffraction pattern of the decomposed phases in Figure S15).

Improved resistance behavior against decomposition was also consistently observed during the reaction with CO_2 at 600 °C for 24 h, demonstrating the crucial advantage of the intergranular-phase-free polycrystals for better chemical durability. As represented in the scanning electron micrographs in Figure S16 in Supporting Information, the decomposed surface layer is significantly reduced to less than two microns in the Ba-deficient sample (right). On the basis of the results of these sets of experiments shown in Figure 6b and Figure S16, suppressing the remarkably reactive intergranular amorphous phases is critical to preventing the serious penetration of gas molecules along grain boundaries and thereby the rapid

collapse of the sintered microstructure. Figure 6c presents schematic illustrations showing the role of a grain-boundary phase as a reactive path in the structural failure of dense polycrystals by moisture and CO_2 gases. Although the reaction at the topmost surface is unavoidable, the highly densified microstructure without intergranular amorphous phases provides the significant advantage of chemical stability as well as proton conduction, as depicted in the illustrations.

The findings in this work have several noteworthy implications regarding the fabrication and stability of $BaCeO_3$ polycrystals. First, our study demonstrates that highly dense polycrystalline $BaCeO_3$ (even >99% in relative density) free of grain-boundary phases can be easily fabricated by conventional sintering at 1350−1400 °C, which is far below the sintering temperatures (>1600 °C) of $BaZrO_3$, without any sintering additives (see Table S1 in Supporting Information). Although overall densification appears to be achieved more easily in the stoichiometric $BaCe_{0.9}M_{0.1}O_{3-\delta}$ samples, presumably due to the liquid-phase-assisted sintering behavior,[36,37] the Ba-deficient $Ba_{0.95}Ce_{0.9}M_{0.1}O_{3-\delta}$ samples show sufficiently high values of relative density (up to 99.4%) when sintered at 1400 °C (see Table S1 for comparison). More importantly, as readily found in the previous literature,[3,7,23,38−40] completely different conductivity values and inconsistent behavior are identified, strongly depending on the type of acceptor dopant and the processing conditions. In contrast, as demonstrated in Figure S17, regardless of the composition of the dopant used in this study, our Ba-deficient $Ba_{0.95}Ce_{0.9}M_{0.1}O_{3-\delta}$ samples free of intergranular phases are noted to consistently show nearly the same values of proton conductivity (1.6×10^{-2} S/cm at 600 °C and 0.9×10^{-2} S/cm at 500 °C on average). It should be noted that these values are also comparable to those of high-conductivity $BaCeO_3$-based polycrystalline perovskites,[13,18,29] even though the grain size of our samples is much smaller (∼0.5 μm) than the size (3−15 μm) reported in previous studies (see the information in Figure S17 for details). Consequently, in terms of achieving better proton conduction in $BaCeO_3$, the suppression of intergranular-phase formation at grain boundaries is likely to be much more influential than the selection of an appropriate acceptor.

As previously reported,[7,41] proton conduction in perovskite oxides is based on two principal processes: rotational diffusion of protons around oxygen and proton transfer between oxygen anions. According to a previous molecular dynamics (MD) simulation,[41] the activation energy of the proton transfer is much larger than that of the rotational diffusion, indicating that the transfer between oxygens is a rate-limiting step for proton conduction. As grain-boundary regions are highly disordered with a relatively low density, the O−O geometry having an irregularly longer distance is inevitably present at grain boundaries, thereby making the proton transfer more difficult. If an intergranular amorphous phase exists, proton transfer is likely to be hindered from this random O−O geometry much more frequently. Note that an MD simulation on the basis of the reactive force field consistently demonstrated this grain-boundary blocking effect against rapid proton conduction in Y-doped $BaZrO_3$.[24] In this regard, the intergranular amorphous phases at grain boundaries should be suppressed to achieve better conduction performance.

Our work demonstrates that structural control of grain boundaries has a notable influence on the overall proton conduction in polycrystalline $BaCeO_3$ in addition to the space charge effect in the grain-boundary regions. Recent reports on a different perovskite oxide, $(Ca_{1/4}Cu_{3/4})TiO_3$,[42,43] have shown that the space charge and relevant dopant segregation at interfaces are remarkably insensitive to the type of interfaces.[44,45] In particular, regardless of whether an intergranular phase exists at grain boundaries or not, nearly identical grain-boundary core structure and the same dopant segregation behavior driven by the space charge were identified at an atomic scale.[45] The space charge distribution in grain-boundary regions in the samples in our study thus does not appear to vary by the presence/absence of intergranular amorphous phases.

Most previous investigations on the decomposition of $BaCeO_3$ focused on small particles with high surface area under unrealistically extreme environments in order for the decomposition reactions to occur within a short period of time. However, based on previous thermochemical calculations and experimental results, moisture does not appear to affect the chemical stability above ∼400 °C, as the formation of $Ba(OH)_2$ is energetically unfavorable at elevated temperature.[23] In addition, an earlier notable demonstration regarding the long-term stability of Sm-doped $BaCeO_3$ showed that there was no significant electrolyte degradation during fuel cell operation in 8% CO_2 + 92% H_2 fuel gas at 800 °C for several months.[19] Therefore, if sufficiently densified polycrystals without grain-boundary amorphous phases are provided along with a proper electrode coating,[46] we believe that $BaCeO_3$ can be a suitable solid-state ceramic membrane offering sufficiently high ionic conduction together with structural sustainability at intermediate temperatures.

In conclusion, the present study has systematically elucidated the strong correlation between the formation of intergranular amorphous phases and the enhancement of proton conduction with improved chemical stability in perovskite $BaCeO_3$. Revealing the presence of an intergranular amorphous phase at grain boundaries, our work demonstrated that the nanoscale grain-boundary secondary phase was not only a major obstacle to rapid proton conduction but also a serious penetration path for H_2O and CO_2 gas molecules facilitating chemical decomposition. Therefore, the fabrication of highly densified polycrystals without the formation of intergranular amorphous phases is of major significance to achieve better ionic transport and microstructural durability in proton-conducting $BaCeO_3$.

■ ASSOCIATED CONTENT

Ⓢ Supporting Information

The Supporting Information is available free of charge on the ACS Publications website at DOI: 10.1021/acs.nano-lett.7b04655.

> Additional STEM images, atomic-scale EDS maps, Nyquist plots for impedance comparison, X-ray diffraction data, optical micrographs for morphology variation, cross-sectional SEM images, schematic illustrations showing fracture behavior, and conductivity comparisons with data reported in previous literature (PDF)

■ AUTHOR INFORMATION

Corresponding Author

*E-mail: sychung@kaist.ac.kr; nalphates@gmail.com.

ORCID Ⓘ

WooChul Jung: 0000-0001-5266-3795

Sung-Yoon Chung: 0000-0002-2260-6201

Notes

The authors declare no competing financial interest.

■ REFERENCES

(1) Iwahara, H.; Esaka, T.; Uchida, H.; Maeda, N. *Solid State Ionics* **1981**, *3-4*, 359−363.

(2) Iwahara, H.; Uchida, H.; Tanaka, S. *Solid State Ionics* **1983**, *9-10*, 1021−1025.

(3) Iwahara, H.; Uchida, H.; Ono, K.; Ogaki, K. *J. Electrochem. Soc.* **1988**, *135*, 529−533.

(4) Schober, T. *Solid State Ionics* **1998**, *109*, 1−11.

(5) Norby, T. *Solid State Ionics* **1999**, *125*, 1−11.

(6) Kreuer, K. D. *Solid State Ionics* **1999**, *125*, 285−302.

(7) Kreuer, K. D. *Annu. Rev. Mater. Res.* **2003**, *33*, 333−359.

(8) Tao, S.; Irvine, J. T. S. *Adv. Mater.* **2006**, *18*, 1581−1584.

(9) Björketun, M. E.; Sundell, P. G.; Wahnström, G. *Phys. Rev. B: Condens. Matter Mater. Phys.* **2007**, *76*, 054307.

(10) Yamazaki, Y.; Blanc, F.; Okuyama, Y.; Buannic, L.; Lucio-Vega, J. C.; Grey, C. P.; Haile, S. M. *Nat. Mater.* **2013**, *12*, 647−651.

(11) Wang, S.; Cheng, Y.; Fang, S.; Zhang, L.; Tang, M.; An, K.; Brinkman, K. S.; Chen, F. *Chem. Mater.* **2014**, *26*, 2021−2029.

(12) Kim, H.-S.; Jang, A.; Choi, S.-Y.; Jung, W.; Chung, S.-Y. *Angew. Chem., Int. Ed.* **2016**, *55*, 13499−13503.

(13) Yang, L.; Wang, S.; Blinn, K.; Liu, M.; Liu, Z.; Cheng, Z.; Liu, M. *Science* **2009**, *326*, 126−129.

(14) Fabbri, E.; Bi, L.; Pergolesi, D.; Traversa, E. *Adv. Mater.* **2012**, *24*, 195−208.

(15) Bi, L.; Boulfrad, S.; Traversa, E. *Chem. Soc. Rev.* **2014**, *43*, 8255−8270.

(16) Duan, C.; Tong, J.; Shang, M.; Nikodemski, S.; Sanders, M.; Ricote, S.; Almansoori, A.; O'Hayre, R. *Science* **2015**, *349*, 1321−1326.

(17) Marrony, M. *Proton-Conducting Ceramics: From Fundamentals to Applied Research*; Pan Stanford Publishing Pte. Ltd.: Singapore, 2016.

(18) Iwahara, H. *Solid State Ionics* **1995**, *77*, 289−298.

(19) Taniguchi, N.; Yasumoto, E.; Gamo, T. *J. Electrochem. Soc.* **1996**, *143*, 1886−1890.

(20) Wu, Z.; Liu, M. *J. Electrochem. Soc.* **1997**, *144*, 2170−2175.

(21) Bhide, S. V.; Virkar, A. V. *J. Electrochem. Soc.* **1999**, *146*, 2038−2044.

(22) Zakowsky, N.; Williamson, S.; Irvine, J. T. S. *Solid State Ionics* **2005**, *176*, 3019−3026.

(23) Matsumoto, H.; Kawasaki, Y.; Ito, N.; Enoki, M.; Ishihara, T. *Electrochem. Solid-State Lett.* **2007**, *10*, B77−B80.

(24) van Duin, A. C. T.; Merinov, B. V.; Han, S. S.; Dorso, C. O.; Goddard, W. A., III *J. Phys. Chem. A* **2008**, *112*, 11414−11422.

(25) Yamazaki, Y.; Hernandez-Sanchez, R.; Haile, S. M. *Chem. Mater.* **2009**, *21*, 2755−2762.

(26) Iguchi, F.; Chen, C.-T.; Yugami, H.; Kim, S. *J. Mater. Chem.* **2011**, *21*, 16517−16523.

(27) Shirpour, M.; Merkle, R.; Lin, C. T.; Maier, J. *Phys. Chem. Chem. Phys.* **2012**, *14*, 730−740.

(28) Clark, D. R.; Zhu, H.; Diercks, D. R.; Ricote, S.; Kee, R. J.; Almansoori, A.; Gorman, B. P.; O'Hayre, R. P. *Nano Lett.* **2016**, *16*, 6924−6930.

(29) Fabbri, E.; D'Epifanio, A.; Bartolomeo, E. D.; Licoccia, S.; Traversa, E. *Solid State Ionics* **2008**, *179*, 558−564.

(30) Bae, K.; Jang, D. Y.; Choi, H. J.; Kim, D.; Hong, J.; Kim, B.-K.; Lee, J.-H.; Son, J.-W.; Shim, J. H. *Nat. Commun.* **2017**, *8*, 14553.

(31) Pergolesi, D.; Fabbri, E.; D'Epifanio, A.; Di Bartolomeo, E.; Tebano, A.; Sanna, S.; Licoccia, S.; Balestrino, G.; Traversa, E. *Nat. Mater.* **2010**, *9*, 846−852.

(32) Zhou, Y.; Guan, X.; Zhou, H.; Ramadoss, K.; Adam, S.; Liu, H.; Lee, S.; Shi, J.; Tsuchiya, M.; Fong, D. D.; Ramanathan, S. *Nature* **2016**, *534*, 231−234.

(33) Chung, S.-Y.; Kang, S.-J. L. *Acta Mater.* **2003**, *51*, 2345−2354.

(34) Luo, J. *Crit. Rev. Solid State Mater. Sci.* **2007**, *32*, 67−109.

(35) Guha, J. P.; Kolar, D. *J. Mater. Sci.* **1971**, *6*, 1174−1177.

(36) Luo, J.; Wang, H.; Chiang, Y.-M. *J. Am. Ceram. Soc.* **1999**, *82*, 916−920.

(37) Nikodemski, S.; Tong, J.; O'Hayre, R. *Solid State Ionics* **2013**, *253*, 201−210.

(38) Shima, D.; Haile, S. M. *Solid State Ionics* **1997**, *97*, 443−455.

(39) Ma, G.; Shimura, T.; Iwahara, H. *Solid State Ionics* **1998**, *110*, 103−110.

(40) Kochetova, N.; Animitsa, I.; Medvedev, D.; Demin, A.; Tsiakaras, P. *RSC Adv.* **2016**, *6*, 73222−73268.

(41) Münch, W.; Seifert, G.; Kreuer, K. D.; Maier, J. *Solid State Ionics* **1996**, *86−88*, 647−652.

(42) Chung, S.-Y.; Kim, I.-D.; Kang, S.-J. L. *Nat. Mater.* **2004**, *3*, 774−778.

(43) Choi, S.-Y.; Chung, S.-Y.; Yamamoto, T.; Ikuhara, Y. *Adv. Mater.* **2009**, *21*, 885−889.

(44) Chung, S.-Y.; Choi, S.-Y.; Yoon, H.-I.; Kim, H.-S.; Bae, H. B. *Angew. Chem., Int. Ed.* **2016**, *55*, 9680−9684.

(45) Yoon, H.-I.; Lee, D.-K.; Bae, H. B.; Jo, G.-Y.; Chung, H.-S.; Kim, J.-G.; Kang, S.-J. L.; Chung, S.-Y. *Nat. Commun.* **2017**, *8*, 1417.

(46) Zakowsky, N.; Williamson, S.; Irvine, J. T. S. *Solid State Ionics* **2005**, *176*, 3019−3026.